

A high resolution interferometric method to measure local swelling due to CO₂ exposure in coal and shale

Pluymakers, A.; Liu, J.; Kohler, F.; Renard, F.; Dysthe, DK

DOI

[10.1016/j.coal.2018.01.007](https://doi.org/10.1016/j.coal.2018.01.007)

Publication date

2018

Document Version

Accepted author manuscript

Published in

International Journal of Coal Geology

Citation (APA)

Pluymakers, A., Liu, J., Kohler, F., Renard, F., & Dysthe, DK. (2018). A high resolution interferometric method to measure local swelling due to CO₂ exposure in coal and shale. *International Journal of Coal Geology*, 187, 131-142. <https://doi.org/10.1016/j.coal.2018.01.007>

Important note

To cite this publication, please use the final published version (if applicable). Please check the document version above.

Copyright

Other than for strictly personal use, it is not permitted to download, forward or distribute the text or part of it, without the consent of the author(s) and/or copyright holder(s), unless the work is under an open content license such as Creative Commons.

Takedown policy

Please contact us and provide details if you believe this document breaches copyrights. We will remove access to the work immediately and investigate your claim.

1 **A high resolution interferometric method to measure local swelling due to** 2 **CO₂ exposure in coal and shale**

3 Pluymakers, A.¹⁾²⁾, Liu, J.^{3,4)}, Kohler, F.¹⁾, Renard, F.^{1,5)}, Dysthe, D.¹⁾

4 1) PGP, University of Oslo, postboks 1048, 0316 Oslo, Norway; 2) Now at Department of Geoscience
5 and Engineering, Delft University of Technology, 2128 CN Delft, Netherlands; 3) Department of
6 Mechanical Engineering, Eindhoven University of Technology, 5600 MB, Eindhoven, Netherlands; 4)
7 Department of Earth Sciences, Utrecht University, 3584 CD, Utrecht, Netherlands; 5) University
8 Grenoble Alpes & CNRS, ISTERre, Grenoble, France

9 **Abstract**

10 We present an experimental method to study time-dependent, CO₂-induced, local topography
11 changes in mm-sized composite samples, plus results showing heterogeneous swelling of coal
12 and shale on the nano- to micrometer scale. These results were obtained using high resolution
13 interferometry measurements of sample topography, combined with a new type of
14 experimental microfluidic device. This device is a custom-built pressure vessel, which can
15 contain any impermeable sample type and can be placed under any microscope. The pressure
16 vessel itself has been tested to handle pressures up to 100 bar at room temperature conditions.
17 For the experiments reported here we used three sample types: i) epoxy and dolomite, ii) coal,
18 epoxy and dolomite and iii) shale. These model systems (thicknesses between 2-10 mm) were
19 exposed to pressurized CO₂ (20-35 bars) and subsequently deformation over time was
20 monitored with a white light interferometer. This provided a lateral spatial resolution of 979
21 nm and a vertical spatial resolution of 200 nm, i.e. sufficient resolution so that coal and shale
22 constituents can be tracked individually. Within 72 hours epoxy swells homogeneously up to
23 11 μm, coal swells 4±1 μm and dolomite is unreactive with the dry CO₂ injected here, and as
24 such is used as a reference surface. The differential swelling of coal can be correlated in space
25 with the macerals, where macerals with an initial higher topography (interpreted to be related
26 to hardness) swell more. The average or bulk swelling exhibits an approximate $t^{1/2}$ relation,
27 indicative of diffusion-controlled adsorption of CO₂ on the organic matter. Measurements of
28 the differential swelling of both shale samples enabled tracking of individual patches of
29 organic matter within the shale (max. 20 × 20 μm). These patches exhibit finite swelling of on
30 average 250 nm in 4 hours (in the Pomeranian shale) and 850 μm in 20 hours (in the Green
31 River shale), where total swelling is assumed to be related to the volume of the patches of
32 organic matter.

33 **Keywords**

34 Enhanced coal bed methane (ECBM); shale gas; CO₂ storage; heterogeneous swelling;
35 surface deformation; time-dependent deformation

36 **Highlights**

- 37 - Versatile method to study local and bulk swelling with nanometer height resolution
38 - The same surface can be imaged with a multitude of microscope techniques
39 - Coal swelling is heterogeneous depending on location. Swelling can vary up to 25%
40 - Finite swelling of local organic matter in shale creates <1 μm high asperities

41 **1. Introduction**

42 Gases such as CO₂ and CH₄ lead to swelling of coal (e.g. Day et al., 2008; Hol and Spiers,
43 2012; Karacan, 2007, 2003; Liu et al., 2015) and shale and clay (e.g. Busch et al., 2016, 2008;
44 de Jong et al., 2014). The heterogeneous deformation of these materials can have opposite
45 effects. It may either inhibit the reactive transport as swelling clogs transport pathways, or
46 enhance reactive transport in those cases where shrinkage creates new transport pathways or
47 when heterogeneous swelling leads to microfracturing. To date, experimental work
48 investigating the permeability and permeability change of a porous medium relied on batch
49 reaction or flow-through set-ups (see Rohmer et al., 2016 for a review of different
50 experimental techniques). Reaction experiments are usually performed in closed pressure
51 vessels, with observation before and after the experiment, i.e. static measurements (for
52 example, Liu et al., 2012). Traditional flow-through experiments capture some of the
53 dynamics of reactive transport, usually by monitoring pressure and chemistry at the in- and
54 the outlet (for example, Bachaud et al., 2011; Edlmann et al., 2013; Elkhoury et al., 2013;
55 Ellis et al., 2011; Olabode and Radonjic, 2014). However, this type of measurements does not
56 provide information where liquid goes, nor on how it interacts with the solid. Over the years
57 different instruments have been used to monitor in-situ fluid-rock interaction using
58 pressurized fluids, such as an eddy current sensor (Hol and Spiers, 2012), in-situ X-ray
59 diffraction (Giesting et al., 2012), regular digital cameras (Day et al., 2008; Perrier et al.,
60 2017), optical microscopy (van Bergen et al., 2009), secondary electron microscopy (Wang et
61 al., 2017), X-ray micro-tomography (Karacan, 2007, 2003; Kobchenko et al., 2011; Nguyen et
62 al., 2013) and microfluidic devices (Neuville et al., 2016; Porter et al., 2015). All of these
63 experimental methods have their own advantages and disadvantages in terms of sample size,
64 resolution, and pressure/temperature/fluid conditions that can be obtained.

65 To image and quantify surface topography changes with submicrometer resolution, we
66 developed a new versatile micro-sized pressure chamber that is suitable for placement under a
67 microscope. The design of our device is such that any type of low permeability reactive
68 material can be inserted and different types of reactive liquids or gases can be used.
69 Moreover, the optical accessibility of the sample allows for observation using various
70 microscopy techniques, including white light interferometry. The latter technique is presented
71 here and it provides nanometer resolution topography measurements of rough surfaces (up to
72 tens of micrometers) by comparing the wavelength, and hence travel path, of a split light
73 beam. Additionally, we developed the accompanying data processing routine necessary to

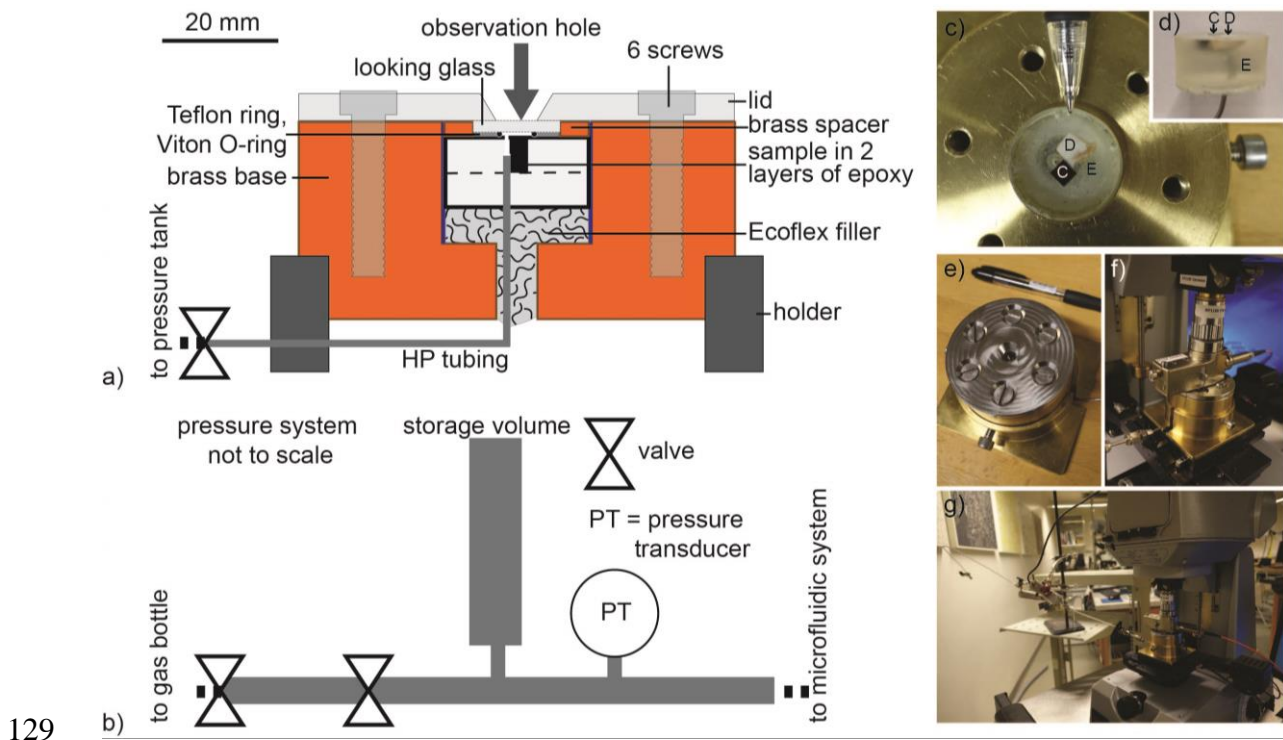
74 register and correct an image time series, which is affected by small lateral drifts of the
75 system. The data processing technique also takes the pixels with incomplete height
76 reconstruction into account. These in-situ white light interferometer measurements allow
77 tracking of the differential surface deformation of various materials in time and space.

78 This new method can be a useful tool for future studies of local reactions that induce surface
79 changes in solid materials under high pressures. It may have impact on diverse industry-
80 related problems, such as corrosion, mineral reactions and coal mining with economic and
81 social implications, especially combined with complementary techniques such as sorption
82 experiments (e.g. Lutyński et al., 2017) or small angle neutron or X-ray scattering
83 (SANS/SAXS) measurements (e.g. Radlinski et al., 2004). Specifically, industry practices
84 such as CO₂ sequestration and/or enhanced hydrocarbon recovery inject high pressure CO₂,
85 captured at power plants, into the subsurface for geological storage and/or enhanced
86 hydrocarbon recovery. Aimed at improving our understanding of reactivity and dynamic flow
87 properties as a result of CO₂-induced swelling in coal and shale gas reservoirs, we report here
88 the results of three types of experiments on materials that react with gaseous CO₂ at room
89 temperature conditions: i) samples with epoxy and dolomite, ii) samples with coal, epoxy and
90 dolomite and iii) samples with shale. These samples were exposed to pressurized CO₂ (20-35
91 bars) and subsequently deformation over time was monitored using white light interferometry.

92 In enhanced coal bed methane, CO₂ is used to enhance methane production (e.g. Moore,
93 2012). In this technique, the coal bed permeability (as determined by the permeability of
94 cleats plus that of the bulk material) is the most important factor determining the ease and
95 efficiency of recovery. Bulk measurements of sorption of methane (e.g. Liu et al., 2017) and
96 ethane (Staib et al., 2014) versus bulk measurements of CO₂ adsorption (e.g. Hol and Spiers,
97 2012) show that if these processes occur in sequence, the competitive sorption will likely lead
98 to shrinkage followed by swelling (already proposed by Brochard et al., 2012). The difference
99 in acquired strain will determine the eventual permeability. Lin et al. (2017) showed that the
100 bulk strain resulting from sorption in a cm-sized core sample is for CO₂ twice that for CH₄.
101 Moreover, bulk measurements have shown that the final swelling rate of different coal types
102 are correlated to maceral content, where vitrinite-rich coals exhibit slower bulk swelling rates
103 (Staib et al., 2014). Furthermore, exposure to CO₂ has been shown to lead to microfracturing,
104 postulated to be related to the differential swelling of different macerals (Hol et al., 2012).
105 Therefore, a method that can successfully capture the dynamic behavior of local macerals
106 plays an important role in better quantifying permeability evolution during enhanced coal bed

107 methane recovery in coal seams. Measuring swelling through visualization of a coal surface
108 captures such local deformation. However, the existing methods have disadvantages, such as
109 low spatial and vertical resolution (10 μm lateral resolution; Day et al., 2008), or the lack of a
110 possibility to image the exact same surface with other microstructural techniques (250 μm
111 voxelsize; Karacan, 2007, 2003). Our technique has an unprecedented submicrometer lateral
112 resolution and vertical nanometer resolution, and the same surface can be imaged as well with
113 other optical microscopy techniques, and electron microscopy.

114 Shale is a strongly heterogeneous rock, with different components that can interact with CO_2
115 with opposite results in terms of permeability. Individual clay minerals are capable of
116 incorporating CO_2 and thus exhibit CO_2 -induced swelling (Busch et al., 2016; de Jong et al.,
117 2014), but it has also been hypothesized that shrinkage occurs if CO_2 leads to dehydration of
118 the mineral structure. Both dehydration and swelling may lead to intercrystalline stresses and
119 hence microfractures (Busch et al., 2016; Ougier-Simonin et al., 2016). Moreover, shales
120 often contain organic matter. Given that coal, i.e. organic matter, exhibits strong swelling
121 upon CO_2 exposure (Hol and Spiers, 2012), CO_2 sorption to organic matter in shale may lead
122 to local swelling as well (cf. Busch et al., 2016). Because of the preferential sorption of CO_2
123 to organic matter over methane, it has also been proposed to use CO_2 for enhanced gas
124 recovery in shale gas plays (Middleton et al., 2015). The competition between swelling,
125 fracturing and permanent CO_2 storage determines the final suitability of a CO_2 storage site
126 versus the use of CO_2 as a fracturing fluid. Note that the heterogeneous swelling behavior of
127 shale has been demonstrated using electron microscopy and exposure to different humidity
128 levels (Wang et al., 2017), but high resolution measurements using CO_2 are lacking.



129
 130 *Fig. 1. a) microfluidic sample assembly; b) pressure system, not to scale; c) top view of*
 131 *dolomite (D)/epoxy (E)/coal (C) sample (used for dolcoal1, 2 and 3), pen for scale; d) side*
 132 *view of c); e) assembled pressure device; f) assembly underneath the white light*
 133 *interferometer; g) assembly plus pressure vessel under the white light interferometer.*

134 2. Materials and Method

135 We measure how sample topography changes over time using a white light interferometer
 136 with a new micro-pressure chamber designed and built at the University of Oslo. The
 137 preparation of the sample, device assembly, procedure and determination of the vertical
 138 resolution of the time series are described below.

139 2.1 Sample preparation

140 The sample of choice is embedded into a 2-component Epofix epoxy. Using epoxy enables
 141 attaching high pressure tubing to any type of sample. To construct the samples, we first
 142 prepare a cylindrical epoxy base of 25 mm diameter and 5-10 mm height that contains the
 143 mm-sized rock sample. Since the window size has a 5 mm diameter, if rock samples are
 144 smaller than 5×5 mm, there will be some reactive epoxy in the CO_2 -exposed area. For such
 145 rock + epoxy samples, repeated use with CO_2 may lead to rock fracture due to epoxy
 146 swelling. After curing, the epoxy base with rock sample is polished until mirror-smooth,
 147 going step-wise up to 4000 grit silicon carbide sandpaper, and finished with a polishing cloth

148 and diamond suspension (1 μm particles). Subsequently we drill the holes for the tubing into
149 the epoxy assembly in two phases: a small diameter (0.6 mm) hole on the sample side, and a
150 larger hole on the other side (1.5 mm; see Figs. 1c; 1d). Before further construction, this base
151 can be imaged with regular optical microscopy and/or electron microscopy (with or without
152 element determination with Energy-Dispersive X-ray Spectroscopy) if needed. After imaging,
153 a high pressure steel tube is roughened with 40 grit sandpaper, and glued in the 1.5 mm hole
154 using brush-on Loctite superglue. The pressure tubing is then fixed with a second epoxy layer,
155 giving a total sample height of 15-25 mm. An example sample containing dolomite and coal
156 in epoxy is shown in Fig. 1c.

157 ***2.2 Pressure vessel construction***

158 The sample is inserted in the brass pressure vessel (Figs. 1a; 1d), with a stainless steel lid with
159 six stainless steel sunken screws and a center hole with 60° edges for microscope access.
160 Below the sample is a soft, donut-shaped, silicone rubber plug (custom-made using Ecoflex
161 00-20, manufactured by Smooth-on), to ensure the sample straightens as the lid is screwed on.
162 On top of the sample rests a 2.45 mm thick donut-shaped brass spacer, encircling a 0.7 mm
163 high Teflon back-up ring and a 5 \times 1 mm Viton O-ring. The glass lid is microscope-quality
164 uncoated H-K9L glass, with a diameter of 15 mm, and a thickness of 1.75 mm. It fits the brass
165 spacer and rests on top of the O-ring which is supported by the Teflon back-up ring. The
166 Teflon back-up ring ensures there will be a micro-pressure chamber between the sample
167 surface and the glass once the O-ring is activated, which is approximately 700 μm high and 5
168 mm in diameter. Nitrile sleeves ensure that the spacer/glass/O-ring assembly remains centered
169 on the sample.

170 The pressure tubing is connected to a pressure system (Fig. 1b; 1f), constructed out of 1/8"
171 tubing, a cm-sized pressure chamber and a WIKA PT-30 pressure transducer. The entire
172 assembly is pressure-tested up to 100 bar using N_2 gas. Since the pressure system is much
173 bigger than the micro-pressure chamber, pressure equilibration between the micro-pressure
174 chamber and the pressure vessel will lead to a stable pressure close to the initial pressure of
175 the pressure vessel. These experiments can thus be performed without a pump. At the used
176 pressures the pressure drop when opening the tap between micro-pressure chamber and
177 pressure vessel is at maximum 1 bar. A potential and simple upgrade of the assembly would
178 be the addition of a pump to ensure a more stable pressure, avoiding the small pressure
179 differences present in our experiments, which were due to minor leakages and room
180 temperature changes.

181 **2.3 Experimental procedure**

182 Sample topography (i.e. pixel height z as a function of position x, y) was measured directly
183 through a glass window by use of a white light interferometer (Wyko NT1100; Fig. 2e; 2f))
184 equipped with a Through Transmissive Media module (Fig. 2e) plus Veeco software. The
185 interferometer is placed on a damped table. Vertical nanometer resolution is achieved for
186 single measurements. In the cases presented here, scanning was performed in vertical
187 scanning mode, using a 20× Veeco objective and a field of view lens of 0.5. The manufacturer
188 specifies that this configuration allows for sampling distances (i.e. pixel size in the height
189 images) of 979 nm, where maximum field of view is $626 \times 426 \mu\text{m}$. Total scan length in
190 vertical scanning mode was up to $50 \mu\text{m}$. The minimum time-lapse measurement interval for
191 this Wyko NT1100 interferometer is ~ 3 minutes. In the experiments presented here the exact
192 time intervals varied from experiment to experiment. They typically ranged from 3 to 5
193 minutes in the first hour of the experiment, to 10, 15 or 30 minutes during the remainder of
194 the experiment. Pressure was logged using the native pressure transducer WIKA software
195 with a 30 or 60 second interval.

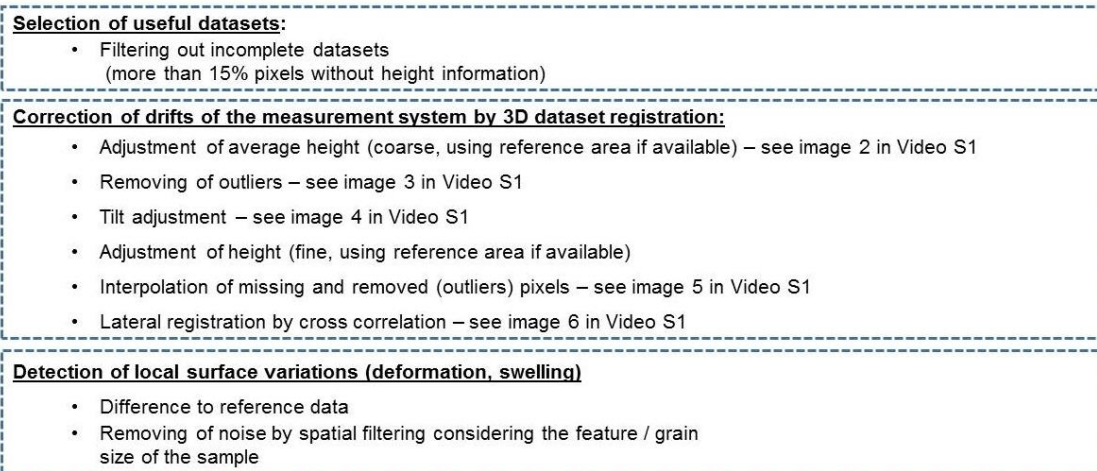
196 Each experiment is preceded by calibration of the vertical scanning imaging mode of the
197 interferometer using a mirror with a $10 \mu\text{m}$ height step. The pressure reservoir is filled with
198 bottle pressure CO_2 gas, and the desired pressure is obtained by stepwise escape of CO_2 . The
199 brass base plus sample are fixed to the white light interferometer stage. A reference glass (10
200 mm diameter, 1.75 mm thickness) is placed in the Through Transmissive Media module, and
201 a duplicate zero measurement is taken whilst the sample is at ambient conditions. The
202 experiment starts by opening the tap between sample and reservoir, pressurizing the micro-
203 pressure chamber between sample and glass.

204 Following adjustment of focus and stage tilt to achieve optimal imaging conditions, the time-
205 lapse imaging sequence is set. Due to drift during long duration experiments (12+ hours),
206 occasionally tilt and/or focus need to be slightly readjusted. Experiments are halted by
207 stopping time-lapse imaging and recording a dual measurement, before pressure is released
208 and pressure logging halted. If desired, it is possible to also record the desorption process and
209 associated shrinkage of the sample.

210 **2.4 Data processing**

211 The raw topography data obtained from the white light interferometer is affected by missing
212 height information, outliers and vertical and horizontal drift of the sample. To determine

213 spatially resolved swelling and shrinkage behavior of the material we developed a data
214 processing procedure, written in Matlab and schematically represented in Fig. 2. The results
215 of the intermediate steps are shown in Video V1 for experiment 3 dolcoal3. Some of the
216 materials observed in this experiment have micrometer topography on the observed interface,
217 such as fractures or pores, as well as a small percentage of dispersed grains with relatively
218 high reflectance. Moreover, the white light interferometer is limited to a certain range of
219 height variations and reflectance for one focal position and one acquisition moment of the
220 camera at the time. Together, this means that the resulting data sets contains pixels at which
221 the height information could not be obtained. As a first step, we dismissed the datasets with
222 more than 15% pixels without height data. The image registration is done in an interactive
223 semi-automated way. First, the datasets are brought to the same plane using the average of a
224 reference area, which is either an inert area (dolomite in our test cases), or the full sample
225 window, i.e. for single material samples (used for the shale samples). In the former case, zero
226 swelling means no reaction at all, i.e. as inert as dolomite is to dry CO₂ exposure. However, in
227 the latter case, only local variations in relative swelling or shrinkage can be distinguished, so
228 no uniform trend of the entire sample area coming up or down can be measured. In this case,
229 zero swelling means just as much reaction as the average surface area. Moreover, if the
230 surface overall swells, the areas that swell less than the average will appear to shrink instead.
231 Apparent shrinkage in such experiments can thus also mean less swelling than the average.
232 After all data is on the same plane, outliers of more than 3x the standard deviation of the
233 comparison of the topography with the median-filtered topography are removed. After
234 removal of tilts using fits to an averaged cross section in *x* and *y* directions, a fine tuning of
235 the vertical axis is performed using the same reference area as used to bring all measurements
236 to the same plane. Subsequently, an estimate of the missing and removed pixel values is
237 gained by interpolation. The lateral data registration is done by cross correlation with a
238 reference dataset taken, e.g., at the beginning of the measurement. Note that with the chosen
239 cross correlation function, cross correlation would be impossible if there was significant
240 lateral motion of the samples throughout the experiment. Finally, time-resolved variations in
241 the surface topography are obtained by subtraction of datasets at successive time steps. Given
242 the fine grain size of clays, for heterogeneous shale plotting the standard deviation of each
243 pixel through time allows determining areas with large relative movement as the areas of
244 interest. Subsequent use of a low-pass filter (with a filter kernel similar to either the grain size
245 of the larger clasts or of individual clay clusters) helps reducing noise and helps to distinguish
246 trends.



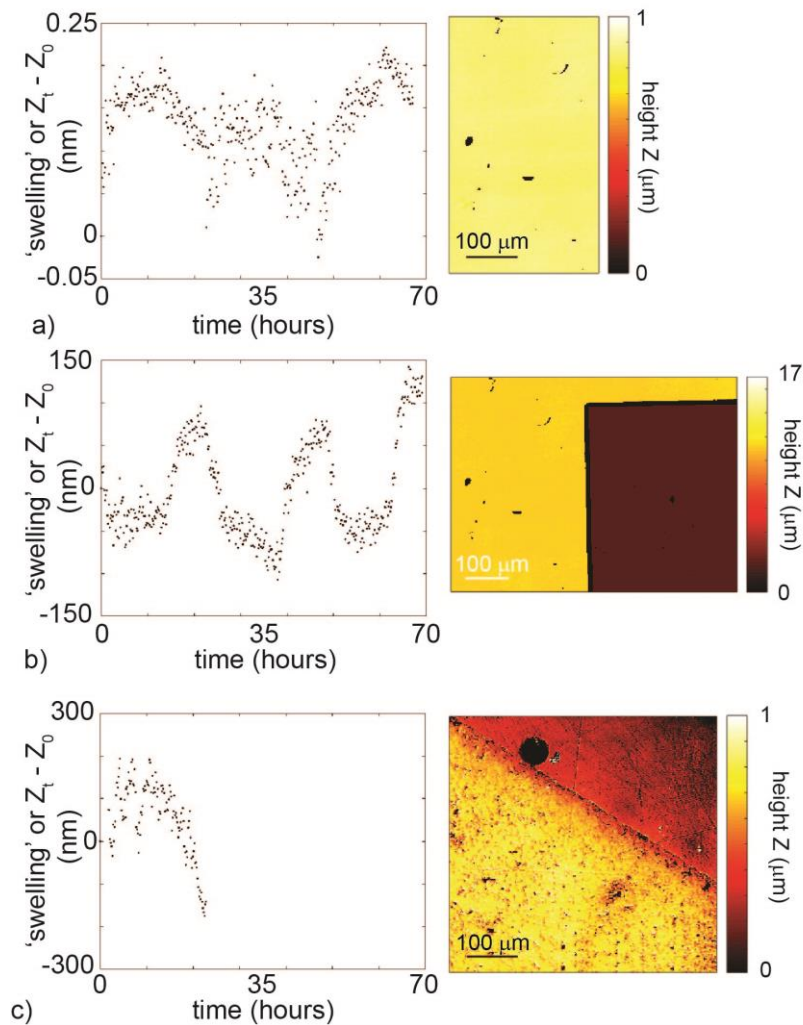
247

248 *Fig. 2. Schematic representation of the different steps of the data processing procedure. See*
 249 *Video V1 for an example (dolcoal 3; the processed data are shown in Fig. 6) how the data*
 250 *evolves with each processing step.*

251 **2.4.1 Vertical resolution of a time-series**

252 Single measurements with this white light interferometer can reach nanometer height
 253 resolution. However, given this nanometer resolution, the measurement of multiple datasets
 254 over time means that small changes in the mechanical parts actually can lead to small drifts,
 255 for example caused by variations in temperature and air currents in the room. The changes in
 256 room temperature also cause small pressure changes in the CO₂ reservoir, leading to
 257 additional movement due to the compressibility of the system. Apart from these reasons for
 258 physical drift, there is also apparent drift due to the presence of unexposed areas. To
 259 determine the combined effect of these factors, we performed a 24 hour measurement of an
 260 inert reference mirror with a 10 μm height step at ambient conditions with time-lapse
 261 imaging, as well as imaging over a dolomite/epoxy interface at ambient conditions. The part
 262 of the mirror surface without steps is measured within nanometer resolution also over time
 263 (Fig. 3a). Note that without topography, there is no possibility to account for any lateral drift,
 264 since this will simply not be registered. Both the averages of the entire mirror (including the
 265 10 μm step) and the dolomite/epoxy interface show a variation of ±100 nm over 24 hours
 266 (Fig. 3b and 3c), due to lateral drift and the noise associated with topography. This means that
 267 the measurement and data-processing procedures as presented here can pick up lateral
 268 differences in swelling that exceed 200 nm. More stable systems and sophisticated analysis
 269 methods (for example, cross-correlation which would allow for subpixel shifts) can further
 270 increase the vertical resolution of this approach. The relatively large field of view (626 × 426

271 μm) combined with the high vertical resolution provides a huge advantage in comparison to
 272 the current techniques which can measure dynamic surface processes. It combines the vertical
 273 resolution of SEM measurements of local swelling in mudrocks (Wang et al., 2017) and the
 274 large lateral extent of measurements of camera observations of coal swelling (Day et al.,
 275 2008).



276

277 *Fig. 3. White light interferometer reference measurements of three different surfaces under*
 278 *ambient conditions. ‘Swelling’ versus time on the right and a map view of the starting*
 279 *topography on the left. ‘Swelling’ is in this case the average topography of the total sample at*
 280 *time t (Z_t) minus the average topography at the starting time (Z_0) versus time, where an*
 281 *increase in height is defined positive (hence swelling); a) a smooth reference mirror (no*
 282 *steps); b) including one $10\ \mu\text{m}$ step and c) of a dolomite/epoxy interface. The oscillations in*
 283 *b) are related to day-night variations in room temperature.*

284 *2.5 Sample-specific methods*

285 The experiments presented here are listed in Table 1. We used dolomite without visible
286 porosity as an inert material for epoxy-swelling tests, i.e. the dolomite was completely
287 surrounded by epoxy. Given that epoxy exhibits strong swelling upon CO₂ exposure and that
288 the geometry of these experiments was simple, they enabled us to develop the data processing
289 routines, plus quantification of the swelling of epoxy. In the other demonstrations tests we
290 used coal and shale as reactive geological materials. The following sample combinations were
291 tested:

292 i) Dolomite / epoxy: not-swelling / large swelling. The dolomite is a pure natural dolomite,
293 obtained from the undeformed wall rock from the Foiana fault zone, Italy. See Fondriest et
294 al. (2015) for a description.

295 ii) Dolomite / coal / epoxy: not-swelling / intermediate, differential swelling / large
296 swelling. The coal sample used in this study was collected from the Brzeszcze mine 364,
297 Poland. It has a vitrinite reflectance of 0.77±0.05%, and is composed of vitrinite (60.1%),
298 liptinite (9.8%) and inertinite (30.1%); ash content is 5.2% (more details in Hol et al.,
299 2011). The coal sample was cut (details in Liu et al., 2016) and subsequently inserted such
300 that the images were taken of the bedding plane; any swelling would hence be
301 perpendicular to bedding.

302 iii) Shale only: heterogeneous behavior. We used two fine-grained, dark grey shale types,
303 both clay-rich and with < 10 % organic matter:

304 ○ Pomeranian shale, fragile core-material (4 km depth) from Poland; see Pluymakers et
305 al. (2017) for a description. This is clay-rich material (50-70% clay + mica, no
306 swelling clays), with up to 10% organic matter. Since this is dehydrated core
307 material, in-situ porosity is impossible to estimate. The images are taken of the
308 bedding plane; any swelling would hence be perpendicular to bedding.

309 ○ Green River shale, strong outcrop material from Utah, see Kobchenko et al. (2011)
310 for a description. In terms of composition this is roughly similar to the Pomeranian
311 shale. Porosity is 5% or less. The images are taken perpendicular to the bedding
312 plane.

313 In the experiments presented here, we used CO₂ gas at maximum 35 bar, since for higher
314 pressures the refractive index changes substantially with pressure (Michels and Hamers,
315 1937). This means that to perform experiments at CO₂ pressures above 35 bar the use of a

316 pump in the assembly is strongly recommended. Note that the procedure described here
 317 would work using any medium (gas or liquid). Due to the non-reversible nature of the epoxy
 318 swelling tests we used new samples in both tests focusing on epoxy (dol2 and dol5). Since
 319 coal swelling upon CO₂ adsorption is nearly reversible after first exposure (Day et al., 2008;
 320 Hol et al., 2012), the coal swelling tests are performed with the same sample (in which the
 321 coal is 3.6 mm thick), even though the epoxy is permanently deformed after the first run.
 322 After each coal swelling experiment this sample is left in a vacuum chamber overnight.
 323 Otherwise, in between runs the samples are kept at ambient conditions. To minimize the
 324 leakage risk, all sample assemblies are pre-pressure tested with N₂ gas and subsequently the
 325 pressure is dropped down for 10-15 minutes using a Busch Zebra vacuum pump (model RH
 326 0006 - 0030 A; pressure of 2.0×10^{-6} bar).

327 *Table 1. Experimental conditions. All experiments are performed in a room with a controlled*
 328 *temperature of $20 \pm 1^\circ\text{C}$.*

Experiment name	Sample	Sample type	Pressure1 (bars)	duration (hours)	Pressure2 (bars)	duration (hours)
Epoxy swelling						
dol2	Dol2	dolomite / epoxy	34 ± 1	41		
dol5*	Dol5	dolomite / epoxy	28 ± 2	1	25 ± 1.2	17 h
Coal swelling						
DOLCOAL1*			27 ± 1	2	20 ± 1	15
DOLCOAL2	Dolcoal1	Dolomite / epoxy / coalcube	25.3 ± 1.2	22		
DOLCOAL3			33.3 ± 1	66		
Shale swelling						
CO2_11	POM_12	Pomerianian shale	31 ± 1	41		
CO2_12	GRS_2	Green River Shale	32 ± 1	44		

329 *These experiments experienced a pressure drop within a few hours after the experiment
 330 started. The pressure steps and their duration are indicated.

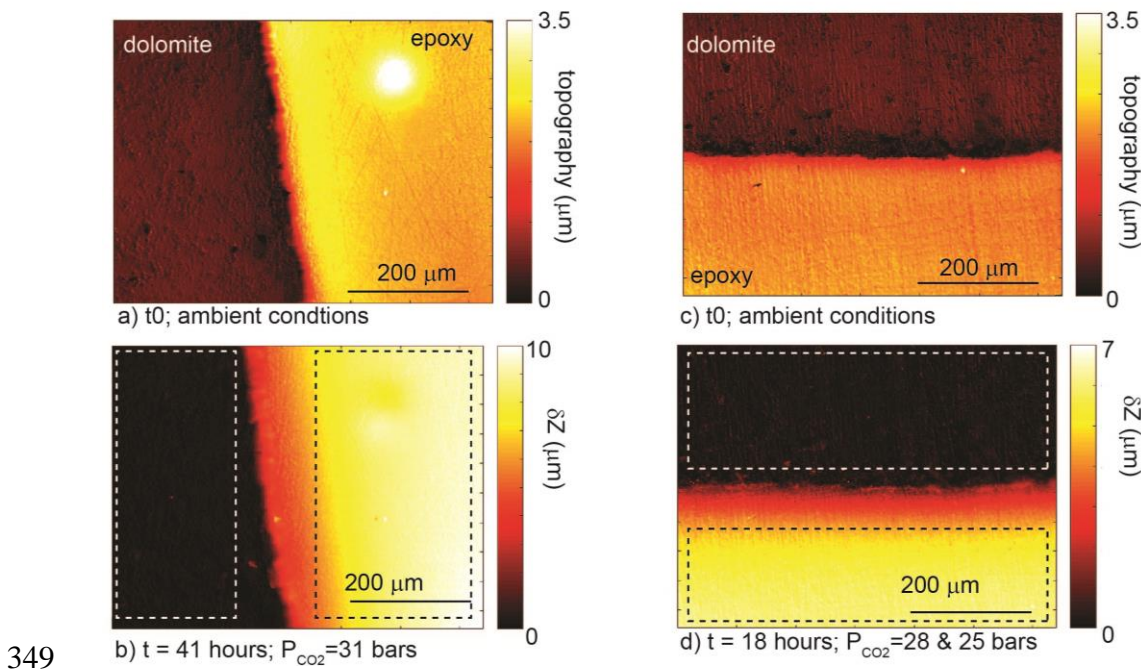
331 **3. Results on local swelling**

332 **3.1 Swelling of epoxy with a dolomite reference: reference experiments**

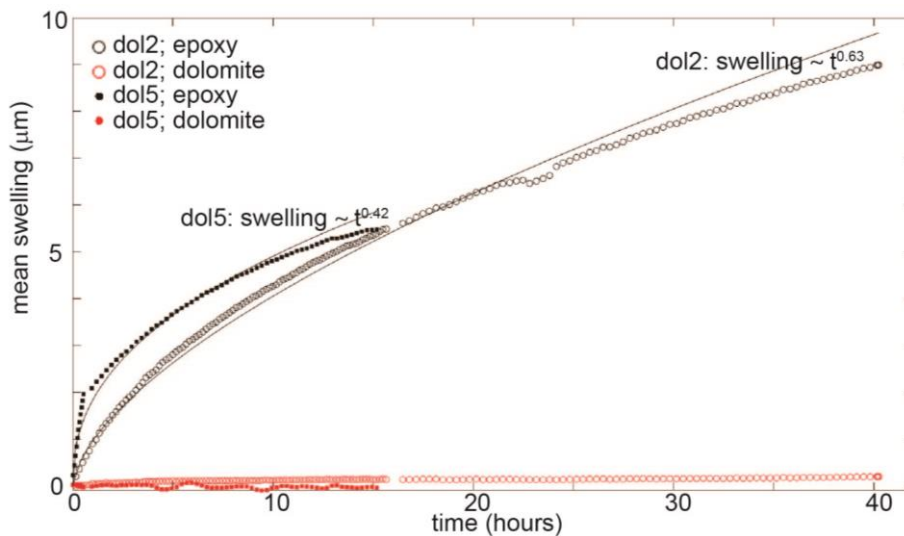
333 To test how measurable swelling is for a simple geometry and to develop the data-processing
 334 protocols, we performed epoxy swelling tests with dolomite as an inert sample (and thus
 335 providing a reference surface). Before CO₂ exposure, the difference in height between
 336 dolomite and epoxy is 3 to 3.5 μm (Fig. 4). Exposure to CO₂ leads to time-dependent non-
 337 uniform swelling of the epoxy (Video V2 on dol2). There is less swelling near the boundary
 338 between dolomite and epoxy because of a no slip boundary condition at this location. At the
 339 end of the experiment the discrete step between the dolomite and epoxy is gradual over 400 –

340 500 μm (Fig. 4). For dol2 the maximum average epoxy swelling is $\sim 9 \mu\text{m}$, and for dol5 this is
 341 $\sim 6 \mu\text{m}$ (Fig. 5). The best fit to the average swelling curve is swelling $\propto t^{0.63}$ for dol2 and
 342 swelling $\propto t^{0.42}$ for dol5, where t is the time from CO_2 gas injection.

343 The time power law exponent close to 0.5 suggests the rate is controlled by Fickian diffusion
 344 of CO_2 into epoxy. For dol5 we performed measurements up to 24 hours after dropping the
 345 CO_2 pressure to atmospheric (not shown), which only showed about $2 \mu\text{m}$ recovery of the
 346 total swelling in this experiment, i.e. most of the deformation is permanent, fitting with
 347 previous polymer research (Busch and Gensterblum, 2011; Day et al., 2008; Wind et al.,
 348 2003).



350 *Fig. 4. Epoxy swelling. See also Video V2, which shows how the surface dol2 swells through*
 351 *time; i.e. the equivalent of Fig. 4b. a) initial map of dolomite and epoxy for sample dol2; b)*
 352 *final differential map of dol2 showing δz (swelling, i.e. the change in surface topography),*
 353 *after ~ 40 hours of exposure; c) initial map of dolomite and epoxy for sample dol5; d) final*
 354 *differential map of dol5 showing δz (swelling), after ~ 16 hours of exposure. Squares indicate*
 355 *areas from which averages are taken that are shown in Fig. 5.*



356

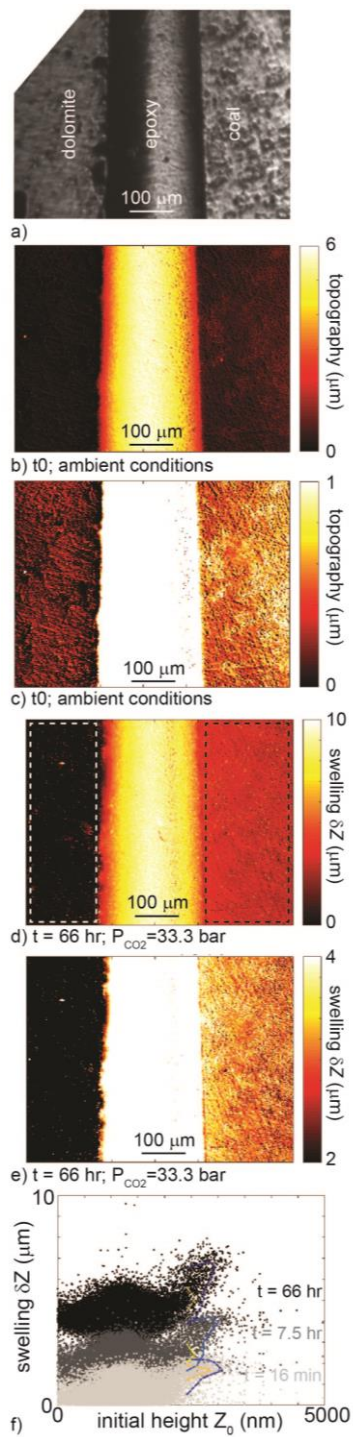
357 *Fig. 5. Average swelling δz (μm) versus time for dol2 and dol5; epoxy in black and dolomite*
 358 *for reference in red. For dol5 there is a 3 bar pressure drop after the first hour (see Table 1),*
 359 *which changed the slope of the swelling curve. The power law fit of the epoxy swelling is*
 360 *shown in black, with the corresponding time exponents.*

361 **3.2 Swelling of dolomite / coal / epoxy**

362 We performed swelling experiments on Brzeszcze 364 coal samples to test the homogeneity
 363 of CO₂-induced swelling of this coal and how the local swelling is distributed in time and
 364 space. This will help constrain the representability of bulk swelling measurements such as
 365 those by Hol and Spiers (2012). The test assembly used here is a sample composed of
 366 dolomite (as a reference), epoxy (glue) and a mm-sized cube of Brzeszcze 364 coal (the
 367 example sample shown in Fig. 1; see also Fig. 6). In the studied area, the intermediate epoxy
 368 is about 300 μm wide. In reflected light, the bedding plane of the coal contains irregularly
 369 shaped structures, interpreted to be different macerals and minerals (Fig. 6a). This structure
 370 creates an initial topography of about 1 μm (Fig. 6b-c). At the end of experiment dolcoal1, the
 371 epoxy bulges out with a maximum height of 5-6 μm with respect to the dolomite and the coal
 372 (Fig. 6b).

373 Exposure to CO₂ leads to swelling of the epoxy and the coal (Fig. 6, Video V3 with the results
 374 of dolcoal3). The epoxy deformation is comparable to the results of dol2 and dol5. Depending
 375 on the experiment, the coal swells between 1.5 and 4.5 μm (always perpendicular to the
 376 bedding; see Fig. 7), and this swelling is fully reversible. Using the thickness of the inserted
 377 coal cube this corresponds to 0.041-0.125% swelling strain. The total swelling depends on
 378 pressure and experiment duration, and swelling exhibits a power law time-dependence with

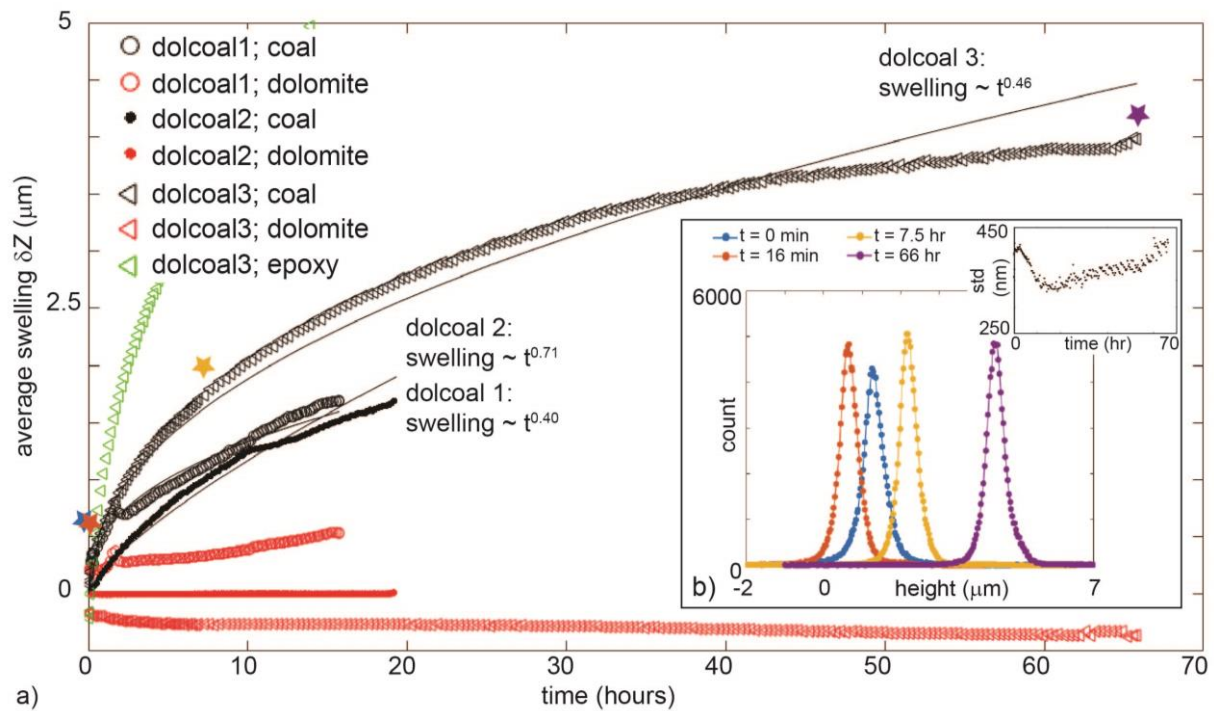
379 exponents between 0.4 and 0.7, see Fig. 7. Studying the results of dolcoal3 in detail (Fig. 6),
380 there is micrometer variability in how much coal swells. This correlates to the initial
381 topography (as can be seen from comparison between Fig. 6c and Fig. 6e, and in Figure 6f),
382 and to the coal surface structure as visible in reflected light microscopy (Fig. 6a). This clearly
383 demonstrates the local heterogeneous swelling properties of mm-sized coal samples, to our
384 knowledge for the first time measured at sub-micrometer lateral resolution. The height
385 distributions (Fig. 7b) show an initial shrinkage of the coal after CO₂ introduction, related to
386 the thermo-elastic effects upon the pressure and temperature change. Taking the evolution of
387 standard deviation of the height with time as a proxy for the coal roughness, there is a slow
388 drop in the first 10 hours (i.e. the surface becomes smoother), after which it recovers (inset in
389 Fig. 7b).



390

391 *Fig. 6. Coal swelling. See also Video V3, which shows the swelling of epoxy and coal through*
 392 *time; i.e. the equivalent of Figs. 6d-f. All three experiments are performed on the same*
 393 *sample. a) reflected light image taken with an optical microscope. There is an irregular*
 394 *pattern in the coal sample of light and dark spots, interpreted to be related to the maceral and*
 395 *mineral content. The bright spots could be the inorganic material (ash content 5.2%). b);c)*
 396 *initial map of dolomite and epoxy for experiment dolcoal3, with different vertical scales to*
 397 *highlight the initial epoxy (b) and coal (c) topography. Coal topography is related to the*

398 morphology visible in a) (interpreted to be the maceral and mineral distribution); d);e)
 399 differential map of dolcoal3 showing δz (swelling), after ~66 hours of exposure. Color scale
 400 for δz in e) is adapted to show the heterogeneous swelling of individual coal macerals.
 401 Squares on d) indicate areas from which averages are taken that are shown in Fig. 7. f)
 402 Initially high macerals exhibit slightly more swelling, shown by the change in angle of the
 403 'tail' compared with the bulk of the data. Contourplots are added to guide the eye.



404 a)
 405 Fig. 7. Average swelling (μm) versus time (hours) for experiments dolcoal1, dolcoal2 and
 406 dolcoal3. These experiments were performed at different pressures, see Table 1. For dolcoal1
 407 there was a 7 bar pressure drop after the first 2 hours (see Table 1), which changed the slope
 408 of the swelling curve. The curve fit of the epoxy swelling is shown in black (time exponents
 409 are indicated in the plot). The stars indicate the timing of the datasets for which the
 410 histograms are shown in b); b) height distributions at different times. Note how the
 411 introduction of CO_2 causes an apparent initial shrinking of the coal. The inset shows how the
 412 standard deviation (std) of the height distributions decreases in the first 10 hours which
 413 indicates an initial smoothing of the surface after CO_2 introduction.

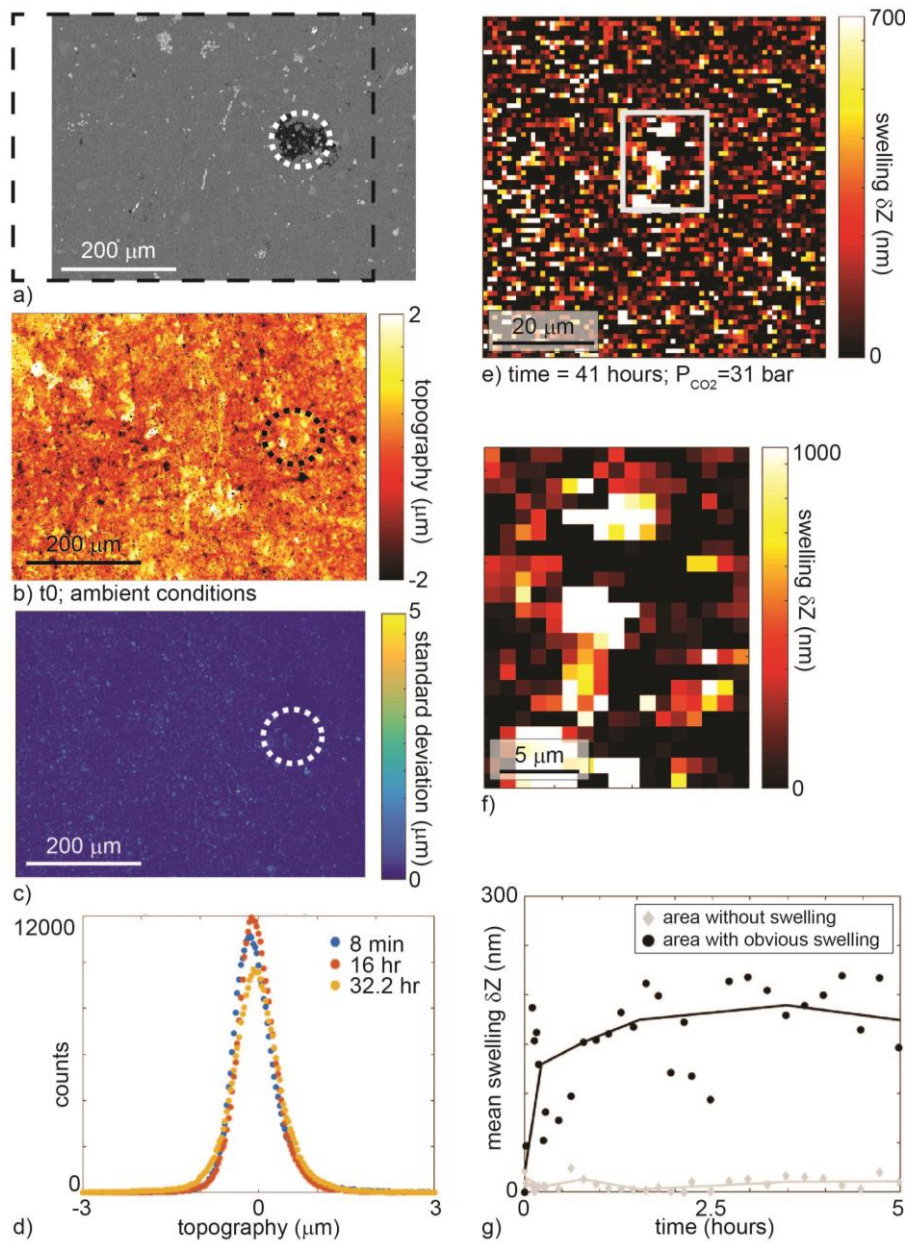
414 3.3 Swelling in shales

415 We also used our set-up to measure CO_2 -induced deformation in the Pomeranian shale and in
 416 the Green River shale (Table 1). In the interpretation of these multiple day exposure

417 experiments it should be taken into account that we are looking at surface effects of 3-D
418 samples, which are semi-confined as a result of the epoxy sample construction. Swelling is
419 hence only possible in the vertical direction. Before the experiments we scanned these
420 samples with SEM and EDS analysis was performed. For the experiments on Pomeranian
421 shale and on Green River Shale we have, respectively, a high (Fig. 8a) and a low resolution
422 (Fig. 9a) backscattered electron image of roughly the same area that is imaged with the white
423 light interferometer. These images are taken with a Hitachi TM3000 (table-top) electron
424 microscope with EDS capability, using a 15 kV acceleration voltage. This allowed
425 identification of an area rich in organic matter, indicated with circles throughout Figs. 8 and
426 10. Even though the samples were polished, the final roughness still contained micron-sized
427 differences between a few recognizable minerals, enabling correlation between the images
428 obtained with secondary electrons (composition, Figs. 8a, 10a) and the white light
429 interferometer (topography, Figs. 8b, 10b). Note that following the CO₂-sorption results on
430 shales with different OM and clay content of Lutyński et al. (2017), we can expect more
431 swelling of the organic matter than of the clay matrix.

432 To first focus on the Pomeranian shale, the total deformation is very small, and not significant
433 in a simple histogram of the topography at different times (Fig. 8c). Therefore, to first identify
434 if there are small-scale local areas with movement, the standard deviation over time for each
435 pixel is plotted in Fig. 8d. There are some mineral shaped areas with high standard deviation,
436 which means these either move up or down. Since each measurement is averaged over the
437 entire sample surface (Fig. 2), if the majority of the surface swells, then those areas that swell
438 less will appear as if they are moving down. Full sample-scale differential map-views of
439 deformation are noisy, due to the fine-grained nature of shale versus the pixel size of 979 nm,
440 i.e. one pixel usually covers multiple particles. Therefore, we focus on the area with organic
441 matter only (which also exhibits a high standard deviation), see Fig. 8e-g. A close-up of this
442 area (Fig. 8e) indicates that within this patch of organic matter + clay + pyrite there is one 20
443 × 20 μm area that exhibits more swelling than the surrounding surface. The average swelling
444 of this area only (Fig. 8f) is compared with the average swelling of the area of Fig. 8e
445 (excluding the data of Fig. 8f) is shown in Fig. 8g. Within the first five hours this area swells
446 250-300 nm, i.e. just above the measurement resolution of a rough surface. After 5 hours
447 swelling stops and the height reaches a steady state value. Note also how the height of the
448 surrounding area exhibits very little change. To clarify the trend, we fitted a moving median

449 for which the time-window is determined through logarithmic binning (Fig. 8g). Fitting a
 450 power-law only to the moving median over the first 4 hours gives a time exponent of 0.37.

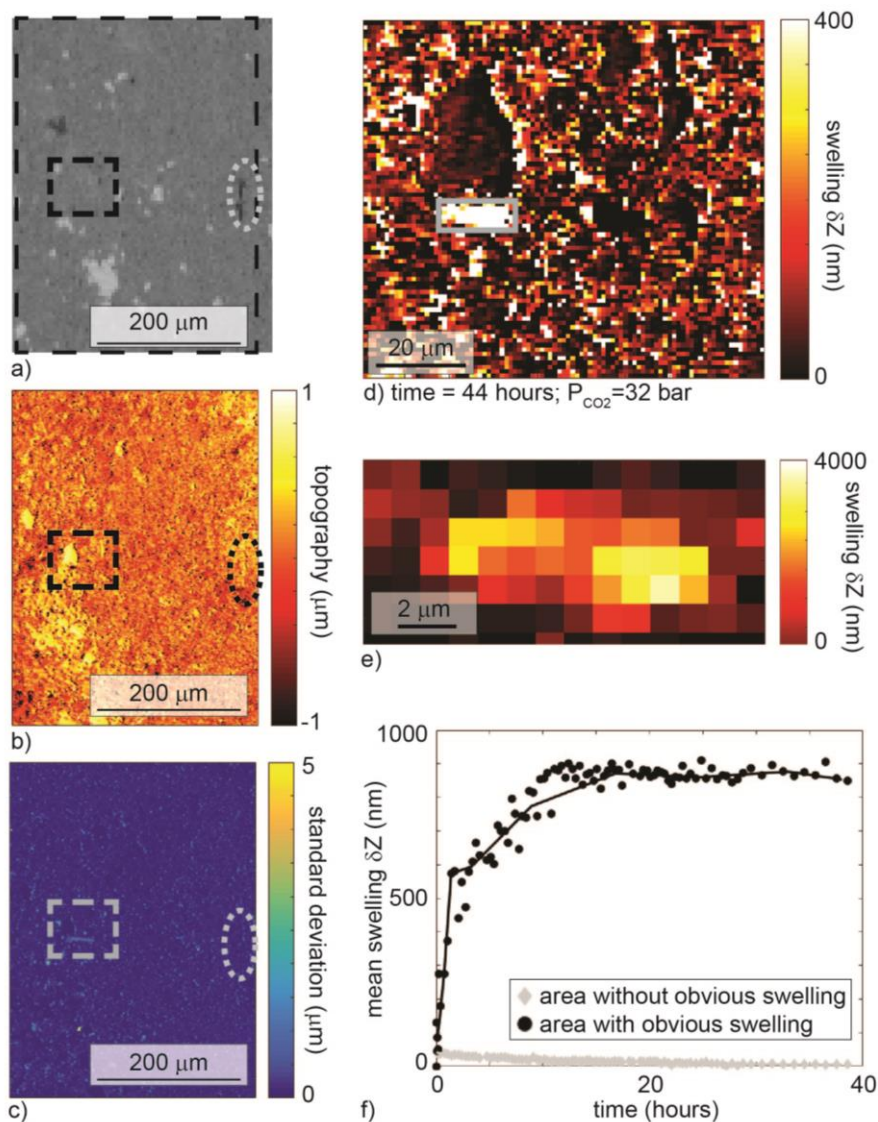


451

452 *Fig. 8. Deformation of sample CO2_11, Pomeranian shale. The circles indicates the location*
 453 *of a patch of organic matter (black), interspersed with pyrite (bright), an area which is*
 454 *investigated in greater detail in Fig. 8e-g); a) backscattered electron image taken before*
 455 *completing sample assembly. The dotted rectangle indicates the approximate location of*
 456 *topography measurements shown in b) where the initial topography is measured with the*
 457 *white light interferometer; c) map with the standard deviation of each pixel through time.*
 458 *High numbers indicate the pixel moved in height during the experiment. In approximately the*
 459 *same location as where the organic matter was present in the SEM image (white circle) there*

460 *are measurable topography changes; d) histogram of the height data at different times. There*
461 *is a small change in the histogram shape, close to the measurement error of 200 nm. 8e-g)*
462 *Close-up of the area containing organic matter; e) a 20 x 20 μm region exhibits more*
463 *swelling than the surrounding shale surface. This is shown in further close-up in f). Note the*
464 *change in scale of the z-axis; g) mean swelling of the area without organic matter and the*
465 *smaller area with organic matter versus time. The solid line is the same data set smoothed*
466 *with a median filter with logarithmic binning of time. On average this patch swells about 250*
467 *nm in the first hours of the experiment.*

468 For the Green River shale, the organic matter visible in the electron image (Fig. 9a) is clearly
469 visible in the topography as a slightly higher area (Fig. 9b). Given the visible organic matter
470 at the surface (and thus easy CO₂ access), some swelling of this region would be expected.
471 However, this area does not exhibit significant swelling (Fig. 9c). This could be related to the
472 small lateral extent of this organic matter patch: it has a high aspect ratio and it is less than 10
473 pixels (or 9.79 μm) wide. This limited lateral extent might be indicative of low thickness, and
474 if the patch of organic matter is too thin there might not be sufficient sorption sites to lead to
475 measurable sorption (>200 nm). In contrast, an elongated patch on the right side of Fig. 9
476 does exhibit high standard deviations (indicated with the dotted box), even though there is no
477 organic matter visible at the surface (Figure 9a). The SEM images of these two shales show
478 that pyrite and organic matter are often found in close proximity (as is also visible in Fig. 8a).
479 This area contains some pyrite, i.e. this unidentified patch of high movement could be an
480 expression of organic matter present just below the surface. The white light interferometer
481 measures relative uplift of the surface only, which in effect is a sum of all processes occurring
482 in the total sample volume as CO₂ diffuses into it. Typical interaction volumes of secondary
483 electron microscopes are on the micrometer-scale, so if there is indeed organic matter below
484 the surface, the swelling force is sufficient to lift a micrometer or more of the shale without
485 fracturing it. A close-up of this area is shown in Fig. 9d-f. There is a small area of
486 approximately 8 x 20 μm that exhibits significant swelling (Fig. 9e; note the 10 \times increase in
487 vertical scale compared to Fig. 9d). This area swells on average about 850 nm compared to its
488 surroundings (Fig. 9f), though locally it reaches 3 μm (Fig. 9e). The total process takes about
489 10 hours, after which the topography reaches a steady height. Fitting a powerlaw to the entire
490 recorded dataset gives a time-exponent of 0.51, but the fit is poor ($R^2=0.61$).



491
 492 *Fig. 9. Deformation of CO₂_12, GRS shale. The dotted circle indicates the elongated patch of*
 493 *organic matter (black) in all images; the squares indicate the area analyzed in Fig. 9d-f; a)*
 494 *backscatter electron image. Bright colors correspond to pyrite grains, and the location*
 495 *imaged with white light interferometry is indicated with the outer black box; b) the initial*
 496 *surface topography as measured with white light interferometry; c) the standard deviation of*
 497 *δZ over time for each pixel. High values indicate the pixel moved over time. There is very*
 498 *little movement in the patch that contains organic matter. There is significant movement of the*
 499 *area analyzed in more detail in Fig. 9d-f; e) a roughly 8 x 20 μm area exhibits more swelling*
 500 *than the surrounding shale surface, despite no obvious organic matter at the surface analyzed*
 501 *with SEM (Fig. 9a). This swelling is shown in further close-up in e) - note the change in scale*
 502 *of the z-axis; f) mean swelling of the area without obvious swelling and the smaller area with*
 503 *obvious swelling versus time. The solid line is the same data set smoothed with a median filter*

504 *with logarithmic binning of time. On average, this small patch swells about 850 nm in the first*
505 *20 hours.*

506 **4. Discussion**

507 ***4.1 Advantages and limitations of the method***

508 Using a novel experimental method we have measured swelling dynamics of a coal and two
509 shale samples upon CO₂ exposure. By tracking the surface movement over time the use of the
510 interferometer provides precise, quantitative data on local deformation and/or how local
511 reactions lead to surface changes in solid materials. The method presented here can measure
512 bulk swelling through averaging over the entire surface, as well as measure local swelling of
513 individual components whilst exposed to a pressurized medium. It has sub-micron lateral and
514 vertical resolution, and the exact same surface can be imaged with a range of microscopes
515 before and after the experiments. Moreover, the current set-up allows the use of different
516 types of swelling-inducing media, provided they are transparent (i.e. different solutions and
517 gases). Finally, the demonstrated method can be applied to any type of composite or initially
518 permeable reactive sample which can be made impermeable with epoxy, a cheap material.
519 Overall, the presented procedure is an extremely versatile and low-cost method.

520 With the set-up presented here, the vertical resolution over time is 200 nm. The vertical
521 resolution is independent of the combination of lenses, and is higher than the resolution of
522 most micro-tomography methods (e.g. Karacan, 2007, 2003; Kobchenko et al., 2011;
523 Pluymakers et al., 2017; Renard et al., 2016). With the lens combination used here, the lateral
524 resolution was 979 nm, i.e. sufficient to identify and track individual minerals and macerals.
525 An obvious generic limitation of microscopy measurements is the trade-off between pixel size
526 and lateral extent of the measurement. The lateral extent of the measurement can be increased
527 by using stitching, the feasibility of which depends on the availability and precision of an
528 automated stage and the measurement speed of the interferometer versus desired sampling
529 rate. In the datasets presented here we used only single (i.e. non-stitched) measurements.
530 Assuming the surface can be imaged without a coating, electron microscopy provides equal or
531 higher lateral resolution (Wang et al., 2017), but it cannot provide high resolution data of any
532 vertical deformation and has more limitations for the type and pressure of swelling-inducing
533 medium to use. An easy improvement to the setup presented here would be the addition of
534 carefully volume-calibrated pressure vessels, include an access to vacuum, and add a precise
535 thermocouple. This would allow simultaneous measurements of bulk sorption and
536 deformation, similar to Karacan (2007, 2003). Since epoxy itself is a reactive material (to CO₂

537 and acetone), for composite samples assembled using reactive epoxy interpretation might
538 prove complicated. The supplementary materials contain further tips and tricks on how to best
539 build and use this assembly.

540 *4.2 Dynamics of coal swelling*

541 We have tracked the bulk swelling behavior of coal, and showed heterogeneity in the swelling
542 behavior of individual macerals. Similar local heterogeneous swelling behavior of coal was
543 also reported by Karacan (2007, 2003) in microtomography experiments with a 250 μm voxel
544 resolution. Note that in their experiments it was not possible to correlate the behavior of the
545 same location one-on-one with observation by other microscopy methods. Moreover, high
546 resolution swelling measurements so far have been mainly measured as bulk-swelling on mm-
547 to cm-sized samples in the laboratory (e.g. Hol and Spiers, 2012). These previous studies
548 report the bulk swelling of a mm-sized Brzeszcze coal sample (i.e. the same coal as used here)
549 exposed to CO_2 at 40°C , using an eddy current sensor with a 50 nm resolution. Comparing
550 their bulk swelling measurements at 3 MPa CO_2 pressure to ours, the average swelling strain
551 experienced by our samples is smaller: $\sim 0.4\%$ by Hol and Spiers vs. 0.13% here, though our
552 samples did not reach full equilibrium yet after 66 hours of CO_2 exposure. First, there is a
553 $\sim 20^\circ\text{C}$ temperature difference. A decrease in temperature would lead to a small increase in
554 swelling, i.e. opposite to what is observed. Second, in our experiments, there is only one
555 exposed face during the experiments. This increases the diffusion path length of CO_2 in the
556 sample. Combined with the passive confinement provided by the epoxy, this will lead to non-
557 equilibrium swelling. Similar non-equilibrium swelling of Brzeszcze coal upon exposure to
558 CH_4 has also been reported by Liu et al. (2016). Third, the sample was kept at ambient
559 conditions in between experiments, and any residual water in coal samples (even atmospheric
560 water) strongly reduces sorption of CO_2 and the associated swelling (Busch and Gensterblum,
561 2011; Day et al., 2008). Even though the current results do not allow for exact determination
562 of the kinetics of swelling, all determined bulk rates all were close to a power law time
563 dependence with an exponent of ~ 0.5 , which, assuming pure Fickian diffusion, would be
564 indicative of a swelling process controlled by the diffusion rate of CO_2 into the matrix. This is
565 in line with studies that show coal sorption and swelling rates to be dependent on sample size,
566 and which accordingly assume diffusion-controlled transport (Busch and Gensterblum, 2011;
567 Gruszkiewicz et al., 2009; Liu et al., 2016; Lutynski and González González, 2016; Staib et
568 al., 2014). The swelling curves presented here are the result of the diffusion of molecules into
569 the sorbent (i.e. the coal), and can be related to diffusive transport models that consider the

570 effects of reversible adsorption processes on the distribution of diffusing models, such as
571 Dumazer et al (2017). Dumazer et al. include an explicit formula for the adsorption flux at a
572 boundary, where the integrated flux would provide the number of molecules adsorbed by the
573 boundary, which should follow the same time-dependence as the swelling surface we
574 measured.

575 The 0.13% swelling strain experienced on average by our samples corresponds to an average
576 swelling of $\sim 4 \mu\text{m}$, where micrometer-sized patches exhibit up to $1 \mu\text{m}$ differences. Local
577 swelling is thus up to $\sim 25\%$ different compared to the average value. This laterally variable
578 swelling followed the geometrical pattern seen in the optical microscopy image (Fig. 6a) and
579 the topography (Fig. 6b; c), which is interpreted to correspond to the composition of the
580 surface, i.e. the macerals and the minerals. Moreover, initially high areas swelled more (Fig,
581 6f). Such heterogeneous swelling supposedly will generate tensile stresses in the coal matrix,
582 and could lead to microcracking (as also postulated by Hol et al., 2012; Liu et al., 2017). This
583 type of microcracks will provide fast transport paths, and should thus accelerate the bulk
584 swelling rate of coal (cf. Hol et al., 2012).

585 ***4.3 Dynamics of heterogeneous deformation in shale***

586 We have measured differential swelling for two different shale types, the Pomeranian and the
587 Green River shales. This type of high resolution differential shale swelling experiments shows
588 some similarity to the experiments performed by Wang et al. (2017). They investigated lateral
589 swelling in clay rocks as a result of exposure to varying air humidity using electron
590 microscopy. Qualitatively, they found similar results as we do: swelling is composition-
591 dependent. In their experiments, water-induced swelling occurs mostly in the clay-rich areas,
592 and not so much in the (larger) carbonate, quartz and pyrite grains. There are two main
593 differences between these experiments. First, we investigated CO_2 -induced swelling in room
594 humidity samples, not humidity-induced swelling in perfectly dry samples. Even though CO_2 -
595 induced clay swelling is expected (Busch et al., 2016; Lutyński et al., 2017), since our method
596 is geared towards measuring differential swelling and not bulk values, this is difficult to
597 capture in these experiments. We choose full shale windows (i.e. without reference surface
598 and epoxy) because of the choice to focus on the differential swelling behavior of organic
599 matter versus that of the clay particles. Second, in the experiments of Wang et al. (2017),
600 lateral movements were captured instead of vertical movement, since their samples were
601 unconfined. The epoxy provides a passive confinement, meaning that the swelling is driven
602 by the diffusion of CO_2 into the matrix so motion here is perpendicular to the surface. That

603 means that if any sorption-induced swelling leads to local surface deformation, our
604 experimental setup can capture it.

605 The preferential CO₂-sorption and associated swelling of patches of organic matter has been
606 hypothesized before, where the process of methane desorption and subsequent CO₂ sorption
607 could lead to enhanced shale gas recovery (cf. Middleton et al., 2015). To our knowledge,
608 these are the first results that capture the dynamics of the swelling process of micrometer-
609 sized patches of organic matter compared to the matrix, for as little swelling as 250 nm. Note
610 that with the current data it is not possible to estimate and compare the swelling strain of the
611 organic matter patches, since their thickness is unknown. We also capture measurable surface
612 deformation (a maximum average of 850 nm) of what supposedly is the expression of organic
613 matter swelling just below the surface. This type of data shows similarity to analogue surface
614 deformation experiments for intrusions, where rate and shape of surface deformation are
615 related to the shape of the intrusion (such as Guldstrand et al., 2017). Combining these
616 methods would enable the determination of the approximate 3D shape of the organic matter.

617 For both shale experiments, there was no clear time dependence for the swelling of the
618 organic matter. The total local swelling possible in shales is finite; in the Pomerianian shale
619 maximum swelling was reached within ~4 hours, and in the Green River shale in ~20 hours.
620 This is easily explained by the finite thickness of the scattered patches of organic matter, from
621 which logically follows there is thus a finite number of sorption sites within each patch of
622 organic matter. Now, assuming a scenario in which CO₂ is used as fracking fluid in shales (as
623 also suggested by Middleton et al., 2015), our results suggest CO₂ adsorption to organic
624 patches can create local, micrometer-sized asperities within the first few hours after opening
625 the fracture. Since these asperities are spatially related to the patches of organic matter, the
626 number and location will be related to the location of organic matter concentrations within the
627 matrix. Moreover, since these patches are limited in extent, the total swelling will be
628 determined to the thickness or size of each patch of organic matter, given that swelling is
629 finite, as also shown in the experiments (Figures 8 and 9). These local asperities might have
630 effects on crack propagation and therefore on the fluid dynamics in the narrow crack tip
631 within the first hours to days after CO₂ exposure. However, in our experiments we showed
632 less than 1 micrometer sized asperities. Sorption-induced swelling of organic matter can be
633 expected to be dependent on the pressure and temperature conditions of CO₂ (similar to coal).
634 However, since typical proppant sizes are up to 500 μm this process should be of minor
635 importance in propped fractures.

636 **5. Conclusions**

637 We have built a working micro-pressure chamber that can hold pressures up to 100 bar, and
638 we used a white light interferometer to directly measure CO₂-induced changes to surface
639 topography for unreactive dolomite, and reactive coals and shale samples. This novel
640 experimental approach allows measuring the dynamics of both bulk and local deformation of
641 the sample while exposing it to fluids at high pressure. The advantages of this set-up lie in the
642 unprecedented submicrometer spatial and vertical resolution, and the versatility with respect
643 to sample and pressurizing medium.

644 We used the presented method successfully to monitor the swelling over time of
645 epoxy/dolomite, coal/epoxy/dolomite and shale samples. Our conclusions are the following:

- 646 - Epoxy swelling is shown to be homogeneous and mostly permanent. It exhibits a standard
647 power law Fickian time-dependence with a time exponent of ~0.5.
- 648 - Swelling of a Brzeszcze coal sample is heterogeneous. Initially higher components exhibit
649 up to 25% more swelling than the average, bulk swelling values. Bulk swelling also exhibits
650 an approximate time-dependence of ~0.5.
- 651 - Measurements targeted at observing local swelling in shales indicate swelling of small,
652 micrometer-sized, patches of organic matter. An average 250 nm swelling in 4 hours is
653 recorded for a 20 × 20 μm patch of organic matter in the Pomeranian shale. For a Green River
654 shale sample, for a 8 × 20 μm location, we record an average 850 nm swelling (though locally
655 this can be 3 to 4 μm) for what is interpreted to be organic matter just below the surface.

656 **6. Acknowledgements**

657 Anne Pluymakers, Dag Dysthe and François Renard are funded by ShaleSeq and the
658 Norwegian Research Council [grant number POL-NOR 234198/100/2014]. Jinfeng Liu is
659 funded by the Darcy Center for porous media research and technology. Felix Kohler is funded
660 by the Norwegian Research Council [grant number 222386]. The funding sources did not
661 influence the study design; the collection, analysis and interpretation of data; in the writing of
662 the report; and the decision to submit the article for publication. We thank the Editor, Ralph
663 Littke, and Sander Hol plus an anonymous reviewer for their comments.

664 **Captions to the Videos**

665 (see published version <https://doi.org/10.1016/j.coal.2018.01.007>)

666 **V1**

667 V1 shows how the topography data (height z as a function of location x, y) evolves as a result
668 from the data-processing routine, which is outlined in Figure 2. Panel 1 shows the raw
669 topography data. This data is not normalized, and there is a significant drift in the zero-plane
670 (hence the 60 μm scale bar for the height). Panel 2 shows the raw topography data after the
671 rough correction in height-scale, using the dolomite as a reference plane. Panel 3 shows the
672 topography data after the outliers have been removed; note the increase in black pixels. Panel
673 4 shows the topography data after the correction for any changes in tilt, and after fine-tuning
674 the height. Panel 5 shows the topography data after the interpolation routine, which filled in
675 all black pixels. Panel 6 shows the topography data after cross-correlation; note that the
676 visible area of the sample is now slightly decreased in size to only show the part for which we
677 obtained a consistent dataset (the drift in the experiments shown in this paper was less than 50
678 pixels). Panel 7 shows the evolution of average height (using the areas as outlined in Fig. 6)
679 with time for the different parts of the sample, i.e. the bulk swelling behavior.

680 **V2**

681 V2 shows the evolution of dol2 over time; processed topography data only. The top left panel
682 is the topography minus the initial topography, where swelling is defined as positive. The two
683 arrows indicate where the profiles are located which are that are shown in the top right panel
684 (parallel to the x -axis) and in the bottom left panel (parallel to the y -axis). The bottom right
685 panel shows how the average swelling evolves with time for the areas as indicated in Figs. 4
686 and 5.

687 **V3**

688 V3 shows the evolution of dolcoal3 over time; processed topography data only. The top
689 panels both contain the same results, the topography minus the initial topography, where
690 swelling is defined as positive. The top left panel contains a height-scale such that the epoxy
691 swelling is completely visible, whereas the top right panel is adjusted to focus on the height
692 evolution of the coal only. This highlights the differential swelling of the coal macerals. The
693 white arrow indicates where the profile shown in the bottom left panel is located; the profile is
694 parallel to the x -axis. The bottom right panel shows how the average swelling evolves with
695 time for the areas as indicated in Figs. 6 and 7.

696

697 **7. References**

- 698 Bachaud, P., Berne, P., Renard, F., Sardin, M., Leclerc, J.P., 2011. Use of tracers to characterize the
699 effects of a CO₂-saturated brine on the petrophysical properties of a low permeability carbonate
700 caprock. *Chem. Eng. Res. Des.* 89, 1817–1826. doi:10.1016/j.cherd.2010.11.004
- 701 Brochard, L., Vandamme, M., Pellenq, R.J.-M., Fen-Chong, T., 2012. Adsorption-Induced
702 Deformation of Microporous Materials: Coal Swelling Induced by CO₂–CH₄ Competitive
703 Adsorption. *Langmuir* 28, 2659–2670. doi:10.1021/la204072d
- 704 Busch, A., Bertier, P., Gensterblum, Y., Rother, G., Spiers, C.J., Zhang, M., Wentinck, H.M., 2016.
705 On sorption and swelling of CO₂ in clays. *Geomech. Geophys. Geo-Energy Geo-Resources* 2,
706 111–130. doi:10.1007/s40948-016-0024-4
- 707 Busch, A., Gensterblum, Y., 2011. CBM and CO₂-ECBM related sorption processes in coal: A
708 review. *Int. J. Coal Geol.* 87, 49–71. doi:10.1016/j.coal.2011.04.011
- 709 Busch, A., Alles, S., Gensterblum, Y., Prinz, D., Dewhurst, D.N., Raven, M.D., Stanjek, H., Krooss,
710 B.M., 2008. Carbon dioxide storage potential of shales. *Int. J. Greenh. Gas Control* 2, 297–308.
711 doi:10.1016/j.ijggc.2008.03.003
- 712 Day, S., Fry, R., Sakurovs, R., 2008. Swelling of Australian coals in supercritical CO₂. *Int. J. Coal*
713 *Geol.* 74, 41–52. doi:10.1016/j.coal.2007.09.006
- 714 de Jong, S.M., Spiers, C.J., Busch, A., 2014. Development of swelling strain in smectite clays through
715 exposure to carbon dioxide. *Int. J. Greenh. Gas Control* 24, 149–161.
716 doi:10.1016/j.ijggc.2014.03.010
- 717 Dumazer, G., Flekkøy, E., Renard, F., Angheluta, L., 2017. Transient anomalous diffusion regimes in
718 reversible adsorbing systems. *Phys. Rev. E* 96, 42106. doi:10.1103/PhysRevE.96.042106
- 719 Edlmann, K., Haszeldine, S., McDermott, C.I., 2013. Experimental investigation into the sealing
720 capability of naturally fractured shale caprocks to supercritical carbon dioxide flow. *Environ.*
721 *Earth Sci.* 70, 3393–3409. doi:10.1007/s12665-013-2407-y
- 722 Elkhoury, J.E., Ameli, P., Detwiler, R.L., 2013. Dissolution and deformation in fractured carbonates
723 caused by flow of CO₂-rich brine under reservoir conditions. *Int. J. Greenh. Gas Control* 16,
724 S203–S215. doi:10.1016/j.ijggc.2013.02.023
- 725 Ellis, B.R., Bromhal, G.S., McIntyre, D.L., Peters, C.A., 2011. Changes in caprock integrity due to
726 vertical migration of CO₂-enriched brine. *Energy Procedia* 4, 5327–5334.
727 doi:10.1016/j.egypro.2011.02.514

- 728 Fondriest, M., Aretusini, S., Di Toro, G., Smith, S.A.F., 2015. Fracturing and rock pulverization along
729 an exhumed seismogenic fault zone in dolostones: The Foiana Fault Zone (Southern Alps, Italy).
730 *Tectonophysics* 654, 56–74. doi:10.1016/j.tecto.2015.04.015
- 731 Giesting, P., Guggenheim, S., Koster van Groos, A.F., Busch, A., 2012. Interaction of carbon dioxide
732 with Na-exchanged montmorillonite at pressures to 640bars: Implications for CO₂ sequestration.
733 *Int. J. Greenh. Gas Control* 8, 73–81. doi:10.1016/j.ijggc.2012.01.011
- 734 Gruskiewicz, M.S., Naney, M.T., Blencoe, J.G., Cole, D.R., Pashin, J.C., Carroll, R.E., 2009.
735 Adsorption kinetics of CO₂, CH₄, and their equimolar mixture on coal from the Black Warrior
736 Basin, West-Central Alabama. *Int. J. Coal Geol.* 77, 23–33. doi:10.1016/J.COAL.2008.09.005
- 737 Guldstrand, F., Burchardt, S., Hallot, E., Galland, O., 2017. Dynamics of Surface Deformation
738 Induced by Dikes and Cone Sheets in a Cohesive Coulomb Brittle Crust. *J. Geophys. Res. Solid*
739 *Earth* in press. doi:10.1002/2017JB014346
- 740 Hol, S., Peach, C.J., Spiers, C.J., 2011. Applied stress reduces the CO₂ sorption capacity of coal. *Int.*
741 *J. Coal Geol.* 85, 128–142. doi:10.1016/J.COAL.2010.10.010
- 742 Hol, S., Spiers, C.J., 2012. Competition between adsorption-induced swelling and elastic compression
743 of coal at CO₂ pressures up to 100MPa. *J. Mech. Phys. Solids* 60, 1862–1882.
744 doi:10.1016/j.jmps.2012.06.012
- 745 Hol, S., Spiers, C.J., Peach, C.J., 2012. Microfracturing of coal due to interaction with CO₂ under
746 unconfined conditions. *Fuel* 97, 569–584. doi:10.1016/J.FUEL.2012.02.030
- 747 Hövelmann, J., Austrheim, H., Beinlich, A., Anne Munz, I., 2011. Experimental study of the
748 carbonation of partially serpentinized and weathered peridotites. *Geochim. Cosmochim. Acta* 75,
749 6760–6779. doi:10.1016/j.gca.2011.08.032
- 750 Karacan, C., 2007. Swelling-induced volumetric strains internal to a stressed coal associated with CO₂
751 sorption. *Int. J. Coal Geol.* 72, 209–220. doi:10.1016/j.coal.2007.01.003
- 752 Karacan, C., 2003. Heterogeneous Sorption and Swelling in a Confined and Stressed Coal during CO₂
753 Injection. doi:10.1021/EF0301349
- 754 Kobchenko, M., Panahi, H., Renard, F., Dysthe, D.K., Malthe-Sørensen, A., Mazzini, A., Scheibert,
755 J., Jamtveit, B., Meakin, P., 2011. 4D imaging of fracturing in organic-rich shales during heating.
756 *J. Geophys. Res.* 116, B12201. doi:10.1029/2011JB008565
- 757 Lin, J., Ren, T., Wang, G., Booth, P., Nemcik, J., 2017. Experimental study of the adsorption-induced
758 coal matrix swelling and its impact on ECBM. *J. Earth Sci.* 28, 917–925. doi:10.1007/s12583-

- 759 017-0778-9
- 760 Liu, F., Lu, P., Griffith, C., Hedges, S.W., Soong, Y., Hellevang, H., Zhu, C., 2012. CO₂-brine-
761 caprock interaction: Reactivity experiments on Eau Claire shale and a review of relevant
762 literature. *Int. J. Greenh. Gas Control* 7, 153–167. doi:10.1016/j.ijggc.2012.01.012
- 763 Liu, J., Fokker, P.A., Spiers, C.J., 2017. Coupling of swelling, internal stress evolution, and diffusion
764 in coal matrix material during exposure to methane. *J. Geophys. Res. Solid Earth* 122, 844–865.
765 doi:10.1002/2016JB013322
- 766 Liu, J., Peach, C.J., Spiers, C.J., 2016. Anisotropic swelling behaviour of coal matrix cubes exposed to
767 water vapour: Effects of relative humidity and sample size. *Int. J. Coal Geol.* 167, 119–135.
768 doi:10.1016/J.COAL.2016.09.011
- 769 Liu, J., Peach, C.J., Zhou, H., Spiers, C.J., 2015. Thermodynamic models for swelling of unconfined
770 coal due to adsorption of mixed gases. *Fuel* 157, 151–161. doi:10.1016/j.fuel.2015.04.070
- 771 Lutynski, M., González González, M., 2016. Characteristics of carbon dioxide sorption in coal and gas
772 shale – The effect of particle size. *J. Nat. Gas Sci. Eng.* 28, 558–565.
773 doi:https://doi.org/10.1016/j.jngse.2015.12.037
- 774 Lutyński, M., Waszczuk, P., Słomski, P., Szczepański, J., 2017. CO₂ sorption of Pomeranian gas
775 bearing shales – the effect of clay minerals. *Energy Procedia* 125, 457–466.
776 doi:https://doi.org/10.1016/j.egypro.2017.08.153
- 777 Michels, A., Hamers, J., 1937. The effect of pressure on the refractive index of CO₂: The Lorentz-
778 Lorenz formula. *Physica* 4, 995–1006. doi:10.1016/S0031-8914(37)80197-4
- 779 Middleton, R.S., Carey, J.W., Currier, R.P., Hyman, J.D., Kang, Q., Karra, S., Jiménez-Martínez, J.,
780 Porter, M.L., Viswanathan, H.S., 2015. Shale gas and non-aqueous fracturing fluids:
781 Opportunities and challenges for supercritical CO₂. *Appl. Energy* 147, 500–509.
782 doi:10.1016/j.apenergy.2015.03.023
- 783 Moore, T.A., 2012. Coalbed methane: A review. *Int. J. Coal Geol.* 101, 36–81.
784 doi:10.1016/j.coal.2012.05.011
- 785 Neuville, A., RENAUD, L., Luu, T.T., Minde, M.W., Jettestuen, E., Vinningland, J.L., Hiorth, A.,
786 Dysthe, D.K., 2016. Xurography for microfluidics on a reactive solid. *Lab Chip*.
787 doi:10.1039/C6LC01253A
- 788 Nguyen, P., Fadaei, H., Sinton, D., 2013. Microfluidics Underground: A Micro-Core Method for Pore
789 Scale Analysis of Supercritical CO₂ Reactive Transport in Saline Aquifers. *J. Fluids Eng.* 135,

- 790 21203. doi:10.1115/1.4023644
- 791 Olabode, A., Radonjic, M., 2014. Diagenetic Influence on Fracture Conductivity in Tight Shale and
792 CO₂ Sequestration. *Energy Procedia* 63, 5021–5031. doi:10.1016/j.egypro.2014.11.532
- 793 Ougier-Simonin, A., Renard, F., Boehm, C., Vidal-Gilbert, S., 2016. Microfracturing and
794 microporosity in shales. *Earth-Science Rev.* 162, 198–226. doi:10.1016/j.earscirev.2016.09.006
- 795 Perrier, L., Plantier, F., Gregoire, D., 2017. A novel experimental setup for simultaneous adsorption
796 and induced deformation measurements in microporous materials. *Rev. Sci. Instrum.* 88, 35104.
797 doi:10.1063/1.4977595
- 798 Pluymakers, A., Kobchenko, M., Renard, F., 2017. How microfracture roughness can be used to
799 distinguish between exhumed cracks and in-situ flow paths in shales. *J. Struct. Geol.* 94, 87–97.
800 doi:10.1016/j.jsg.2016.11.005
- 801 Porter, M.L., Jiménez-Martínez, J., Martínez, R., McCulloch, Q., Carey, J.W., Viswanathan, H.S.,
802 2015. Geo-material microfluidics at reservoir conditions for subsurface energy resource
803 applications. *Lab Chip* 15, 4044–53. doi:10.1039/c5lc00704f
- 804 Radlinski, A., Mastalerzb, M., Hinde, A., Hainbuchner, M., Rauch, H., Baron, M., Lin, J., Fan, L.,
805 Thiyagarajan, P., 2004. Application of SAXS and SANS in evaluation of porosity, pore size
806 distribution and surface area of coal. *Int. J. Coal Geol.* 59, 245–271.
807 doi:https://doi.org/10.1016/j.coal.2004.03.002
- 808 Renard, F., Cordonnier, B., Dysthe, D.K., Boller, E., Tafforeau, P., Rack, A., 2016. A deformation rig
809 for synchrotron microtomography studies of geomaterials under conditions down to 10 km depth
810 in the Earth. *J. Synchrotron Radiat.* 23, 1030–1034. doi:10.1107/S1600577516008730
- 811 Rohmer, J., Pluymakers, A., Renard, F., 2016. Mechano-chemical interactions in sedimentary rocks in
812 the context of CO₂ storage: Weak acid, weak effects? *Earth-Science Rev.* 157, 86–110.
813 doi:10.1016/J.EARSCIREV.2016.03.009
- 814 Staib, G., Sakurovs, R., Gray, E.M., 2014. Kinetics of coal swelling in gases: Influence of gas
815 pressure, gas type and coal type. *Int. J. Coal Geol.* 132, 117–122. doi:10.1016/j.coal.2014.08.005
- 816 van Bergen, F., Spiers, C., Floor, G., Bots, P., 2009. Strain development in unconfined coals exposed
817 to CO₂, CH₄ and Ar: Effect of moisture. *Int. J. Coal Geol.* 77, 43–53.
818 doi:10.1016/j.coal.2008.10.003
- 819 Wang, L.L., Yang, R.W., Chanchole, S., Zhang, G.Q., 2017. The time-dependent swelling of
820 argillaceous rock under resaturated conditions. *Appl. Clay Sci.* 146, 186–194.

821 doi:10.1016/j.clay.2017.05.041

822 Wind, J.D., Sirard, S.M., Paul, D.R., Green, P.F., Johnston, K.P., Koros, W.J., 2003. Relaxation
823 Dynamics of CO₂ Diffusion, Sorption, and Polymer Swelling for Plasticized Polyimide
824 Membranes. *Macromolecules* 36. doi:10.1021/MA034359U

825 Supplementary Information

826 This document consists of two parts. Part S1 contains helpful tips, mostly regarding sample
827 assembly. Part S2 contains a few adaptations we would consider changing if we would
828 construct this pressure assembly again.

829 **S1. Helpful tips to reproduce these experiments**

- 830 - Before each experiment, clean the reference glass with a non-corrosive cleaner and
831 blow off the liquid with pressurized air to avoid residual stains. The cleaner the glass
832 (also the reference glass) the higher the data quality.
- 833 - Change the Teflon backup rings before each experiment.
- 834 - The nitrile sleeves used here are the fingers of used lab gloves, size L.
- 835 - If you make the top epoxy + sample layer too thin (< ~ 5mm) then it becomes difficult
836 to drill two holes without breaking it. If you make it too thick (> ~ 15 mm) then the
837 top layer is not strong enough to grip the pressure tubing and the assembly will leak
838 along the tubing.
- 839 - Do not apply any shear force on the pressure tubing, the grip between pressure tubing
840 and epoxy is the weakest point of the assembly.
- 841 - If you make a window with only rock (such as the shale windows) the rock needs to be
842 only a few mm thick, since it is difficult to drill through without creating
843 microfractures. If fractured, the microfractures will provide an easy pathway out of the
844 pressure chamber.
- 845 - Use a diamond drill to drill through rock samples.
- 846 - Whether the assembly holds pressure or not depends a lot on the exact thickness of the
847 soft filler. First we did it by trial and error, but if the filler is too thick you either break
848 the glass during tightening the lid, or you get creep and/or stick-slip behavior of the
849 filler once the pressure is applied and the sample might drop out of focus. If the filler
850 is not high enough, the O-ring is not properly activated once the lid is tight and the
851 assembly leaks. The lengths of filler plus sample that worked for these assembly

- 852 dimensions are 23 – 25 mm. Keep the correct length filler with each sample, to avoid
853 searching for them every time.
- 854 - Note that the Ecoflex-fillers loose some liquid due to the tightening, making them a
855 little stiffer each time you use them. Eventually they become a little too short, and they
856 need replacing.
 - 857 - The filler edges do not need to be perfectly parallel.
 - 858 - Short fillers (and thus long samples) work better than using long fillers (i.e. short
859 samples), since it decreases the chance of filler creep.
 - 860 - Pre-test each filler/sample combination using a non-reactive gas (in the cases
861 presented here N₂) to avoid starting the reaction with a leaking assembly.
 - 862 - Ensure that the lid is straight using a level during tightening. Tighten opposite screws,
863 moving either clockwise or anticlockwise. If not, the microscope stage has to be tilted
864 too much and you run out of space when finding focus and/or you cannot get nice
865 wide interference fringes.
 - 866 - Fixing the sample vessel to the microscope stage was done with cross-linked double-
867 sided tape, plus additional regular tape securing the edges. This worked as long as the
868 distance between the pressure vessel and the stage was such that the tubing did not
869 exert a pull or push on the sample assembly.
 - 870 - If there is a push/pull from the pressure vessel or creep in the filler, it shows up when
871 running a scan that uses the average of multiple scans to calculate pixel height. The
872 resulting image will be fuzzy. If it is filler creep you can still run time-step scans (until
873 the sample drops out of focus), just not averaged ones.
 - 874 - The drift in the z-axis of the white light interferometer requires either a sample where
875 the average height of the sample is not expected to change, or a reference which can
876 be assumed to be always the same height.
 - 877 - Data-processing: each experiment has a different measurement after which the
878 pressure is stable enough to use the measured dataset as a reference. Adapt starting
879 time.
 - 880 - Keep the code for each experiment so you do not have to write down all parameters
881 and you do not have to save the processed data (due to file-size).

882 **S2. Things we would change if we would construct another device**

- 883 - Use a slightly stiffer filler.

- 884 - Make the lid a little thinner, to allow a little tilt and/or filler creep without losing
885 focus.
- 886 - Use a pump to keep pressure, since small leaks are difficult to avoid with the 1/16”
887 tubing.
- 888 - Try to use 1/8” pressure tubing all over, though diameters of the holders need to be
889 adjusted and the total volume in the assembly will increase substantially.
- 890 - If not using a pump, think about the geometry of the large pressure vessel. This long
891 assembly was now made with the idea of being able to go to higher CO₂ pressures by
892 cooling part of the assembly during CO₂ injection, and then slightly heating the entire
893 assembly, following (Hövelmann et al., 2011). The current geometry of the pressure
894 system was impractical to handle and carry around the lab.
- 895 - Do not use Teflon as a back-up ring, since repeated assembly and de-assembly leads to
896 slight widening of the inner diameter and insufficient compression of the O-ring.